# Developing Realistic FDTD GPR Antenna Surrogates by Means of Particle Swarm Optimization

Sam Stadler and Jan Igel

***Abstract*— The antenna is the most important part of a ground-penetrating radar (GPR) system and defines the employed electromagnetic pulse and how it is transferred to the ground. It is crucial to account for these coupling effects in numerical simulations and to implement realistic antenna models, e.g., for full-waveform inversion (FWI). We present a method of developing and adapting 3-D finite-difference time-domain (FDTD) models of GPR antennas, complete with electric components, dielectric material properties, and feed pulse details. We exemplify this with a commercially available, shielded 400 MHz GPR antenna, a model of which was set up by fitting synthetic data to an experimental signal of the antenna reflected at a metal plate in the air. For this FWI, we used a particle swarm optimization (PSO) algorithm because the fit parameters show complex individual effects on the GPR waveform. The resulting antenna model is then validated against data measured in air, water, and with a metal plate in the near field of the antenna. Overall, the synthetic data reproduce the validation data very accurately. Signals of objects placed in the near field of the antenna and the change of the shape and frequency content of the radiated wavelet with varying subsurface properties are emulated correctly.**

***Index Terms*— Electromagnetic (EM) propagation, finite difference methods, geophysics computing, ground-penetrating radar (GPR), particle swarm optimization, ultrawideband antennas.**

## I. Introduction

GROUND-PENETRATING radar (GPR) is a geophysical measurement tool that has a broad application spectrum in geoscience and engineering with variations of targets, exploration depth, and instrument configurations [1]. It is commonly used for high-resolution, near-surface investigations. The GPR method uses electromagnetic (EM) waves, with frequencies ranging from 1 MHz up to 4 GHz, to image structures that are related to changes in the dielectric and electrical properties of the subsurface. This is not limited to geologic materials and can, among others, include asphalt, concrete, ice, and wood [2].

Numerical simulations of GPR scenarios have been used in the past to study various aspects of GPR measurement scenarios. This includes, e.g., the optimization of measurement configurations [3] and the processing and analysis strategies for time-lapse GPR data [4]. Furthermore, complex EM wave phenomena were investigated, such as the dispersion characteristics of subsurface GPR waveguides [5] and the influence of a complex subsurface on GPR signals, such as fine-layered sediment sequences [6], subsurface heterogeneity [7], [8], or dispersive soil properties [9]. Finally, numerical simulations are also the basis of inversion techniques of GPR data, such as full-waveform inversion (FWI) of GPR crosshole data [10]. There are a couple of numerical methods used for the simulation of EM wave propagation, such as the method of moments, finite elements, and finite-difference time domain (FDTD). The latter is widely used for GPR due to its flexibility in modeling and operation in the time domain and, thereby, its ability to include a broad range of frequencies with one simulation. Also, modern FDTD software packages are able to keep the total size of the models relatively small by means of minimizing unwanted energy reflections from the finite grid borders [11], [12]. As the name implies, the FDTD method uses a finite-difference grid that is staggered in time and space to compute Maxwell's equations [13].

When performing numerical studies of scenarios where antenna coupling and near-field effects appear, it is important to include 3-D antenna models in the simulations for the following reasons. In GPR scenarios with shallow targets and complex subsurfaces, the majority of the transmitted energy interacts and moves within the near field and, in particular, within the reactive near field of the antenna [14]. When the subsurface material properties are inside the near field of the antenna change, so do the antenna characteristics, ground coupling, and the emitted wavelet. GPR antennas are usually placed on the ground, and often targets are situated in the near field of the antenna. This results in a complex EM wave field in the immediate vicinity of the antenna. Another effect that can only be emulated by realistic 3-D antenna models is multiple reflections of waves bouncing back into the subsurface at the bowties or metallic shield of the antenna. However, using 3-D models of complex GPR antennas for numerical simulations has only recently been introduced [15], [16]. This is mainly because, when simulating in 3-D and for a uniformly spaced grid, this means adopting a very fine mesh discretization ($<$3 mm), which is necessary for accurately implementing the geometry and the electrical components [17], [18], resulting in a great computational effort. Up until now, there is a lack

Manuscript received July 14, 2021; revised December 2, 2021; accepted December 20, 2021. Date of publication January 19, 2022; date of current version June 13, 2022. This work was supported by the German Federal Ministry of Defence under Project C/E520/HF022/EF120 and Project C/E520/IF008/JF005. *(Corresponding author: Sam Stadler.)*

The authors are with the Leibniz Institute for Applied Geophysics, 30655 Hannover, Germany (e-mail: sam.stadler@leibniz-liag.de).

Color versions of one or more figures in this article are available at https://doi.org/10.1109/TAP.2022.3142335.

Digital Object Identifier 10.1109/TAP.2022.3142335

of numerical models of GPR antennas, especially those of mid-range and lower frequencies (<1 GHz), which are commonly used in geoscientific and civil engineering applications (e.g., [19]). This is due to finding a compromise between resolution and depth of investigation. The electric properties of most geological materials are affected by the presence of free water and its relaxation characteristics that cause an increased effective conductivity and reduced permittivity at higher frequencies [20]. In the frequency range between 10 and 500 MHz, the dispersion and attenuation of the EM waves are the lowest. This is the frequency range called GPR plateau, which typically ensures the best GPR performance. Another factor is scattering losses that strongly increase with higher frequencies. An accurate antenna model will enable more accurate simulations for a range of different purposes. For one, any application where the signal source is in the near-field vicinity of any other medium would profit from using a full antenna model as the near-field effects would implicitly be simulated correctly. Furthermore, the correct evaluation of signal amplitudes would also benefit from the usage of an antenna model, where the correct amplitude ratio between crosstalk and the transmitted signal would be inherent. Finally, applications such as FWI where a GPR source signal has to be guessed would no longer have that need as the antenna model would correctly simulate the near-field interaction between the antenna and the surrounding material properties.

Simplified GPR sources have long been used in the past for a diverse number of applications, e.g., inverse scattering problems [21], [22]. Early works [23]–[26] have focused on implementing simple antenna types and/or parts of antenna models that do not yet include all antenna components. Recent works have progressed to using more geometrically/electrically accurate antenna models, including, e.g., the shielding and absorber materials [16], [27]–[30]. The difficulty with implementing antenna materials in the simulations is to find accurate parameter values that reliably reproduce the measured signals and antenna coupling effects. Generally, little to no information is available for materials used in commercially available antennas. Different approaches have been used to obtain sets of suitable material parameters. Warren and Giannopoulos [16] used the Taguchi optimization method [31] to optimize the antenna crosstalk, while Giannakis *et al.* [30] used a linear/nonlinear FWI to optimize the antenna crosstalk and the signal from an antenna that is directly coupled to a metal plate. In both works, antennas with frequencies above 1 GHz were used.

The computing capabilities of FDTD forward calculation strongly increased in the last years due to advancements in hardware and software, such as code parallelization and the use of high-performance GPUs. This now allows the use of global metaheuristic optimization methods, e.g., particle swarm optimization (PSO), for computationally expensive problems involving 3-D GPR antennas. PSO has the advantage of simplicity, fast convergence rate, ability to tackle ill-posed and nonlinear problems, being little sensitive to local minima, and not relying on *a priori* information and its ability to find a global optimized solution [32]–[34]. PSO has been used in the past in various geophysical fields to perform inversion studies of magnetotelluric, dc resistivity, and induced polarization (IP) data [35]–[37]. In the realm of wave methods (seismics and GPR), PSO algorithms have been applied to joint GPR and P-wave travel-time inversion, crosshole travel-time tomography, Scholte-wave inversion, or the identification and characterization of buried objects from constant-offset GPR [38]–[45].

In this article, we present a performant approach to create numerical 3-D antenna models. In contrast to previous works, which optimize the antenna crosstalk and signals from antennas directly coupled to a metal plate, we optimize the emitted wavelet by means of analyzing the distant reflection at a metal plate. Furthermore, we implement an antenna in the mid-frequency range, while, so far, only antennas with frequencies above 1 GHz have been modeled. Important to keep in mind is that, with decreasing frequency and, consequently, increasing wavelength and antenna size, it becomes more difficult to have full control over the experimental setting and collect clean data without disturbances from, e.g., side reflections. We developed a numerical model of a shielded commercially available 400 MHz GPR antenna that emits accurate wavelets in different kinds of media. First, the 3-D geometry of the main antenna components (bowties, metallic shield casing, absorber foam, and so on) is implemented in the FDTD model. Then, the corresponding material properties are found via fitting synthetic data to reference data of a controlled experiment by a PSO optimization algorithm. Finally, we validate this antenna model by comparing simulated and measured traces in different scenarios and subsurface media.

## II. Methods

The GPR measurements that provided the reference data were performed with a shielded 400 MHz nominal center frequency antenna (model 50400S, S.N.: 1536) and an SIR 4000 apparatus, both from Geophysical Survey Systems Inc. (GSSI). Raw data were acquired without applying any filter. Prior to all measurements, the system was switched on for 15 min to warm up and to reduce any temporal drift of the signal. The center frequencies of the antenna while placed in air ($\varepsilon_r = 1$) and on water ($\varepsilon_r = 82$) were measured to be ≈500 and ≈300 MHz, respectively. This corresponds to wavelengths $\lambda_{air} \approx 0.6$ m and $\lambda_{water} \approx 0.11$ m.

For the numerical simulations of the GPR scenarios, we used the open-source FDTD software package gprMax [46]. It is an established open-source software package that allows to set up extensive and complex models for GPR problems. It contains features that allow for fast modeling and simulation via tools such as perfectly matched layer (PML) boundaries, which efficiently minimizes boundary reflections [47], and the usage of parallel computation on GPUs [48], which significantly speeds up the simulation. We performed the simulations on an NVIDIA RTX 8000 GPU with 48 GB of RAM.

The goal of our optimization problem is to find a set of parameter values that minimize the fitness function, in our case, the relative root mean square error (rel. RMSE) between the amplitude values of the measured and simulated GPR

traces

$$\text{rel. RMSE} = \frac{\|\mathbf{d} - \mathbf{G}(\mathbf{m})\|_2}{\|\mathbf{d}\|_2} \tag{1}$$

where "$\mathbf{d}$" represents the measured data, "$\mathbf{G}$" the forward operator, i.e., the FDTD calculation, "$\mathbf{m}$" the model parameters, and $\|_2$ the L2 norm. To solve the optimization problem and find values for the antenna model parameters, we used the PSO method [49]–[51]. It uses a fixed population of particles (called a swarm) that each represents a possible solution to the given problem to iteratively find a global optimal solution. In the PSO algorithm, each particle represents one set of parameter values $\mathbf{p}$, which lie within predetermined boundaries. Every particle maintains the memory of its overall personal best position $Pbest$ and velocity $\mathbf{v}_i$. Within each generation, the particle velocities are updated jointly with their personal best positions $Pbest$ and the position of the globally best particle in the whole swarm $Gbest$ with regard to the fitness function. The new velocities are then used to compute the new optimal positions for each particle. Over time, the particles move toward more promising regions within the parameter space. The velocity update formula is given by (2), and the position update formula is given by (3)

$$\mathbf{v}_i^{k+1} = w\mathbf{v}_i^k + c_1 r_1\left(Pbest_i^k - \mathbf{p}_i^k\right) + c_2 r_2\left(Gbest^k - \mathbf{p}_i^k\right) \tag{2}$$

$$\mathbf{p}_i^{k+1} = \mathbf{p}_i^k + \mathbf{v}_i^{k+1} \tag{3}$$

where the index $i$ denotes the particle, the index $k$ denotes the iteration, $r_1$ and $r_2$ are random numbers in $[0, 1]$, $w$ is the inertia weight, and $c_1$ and $c_2$ are the "cognitive" and "social" scaling factors, respectively. Setting $w$, $c_1$, and $c_2$ needs to be done in accordance to the problem at hand, largely depending on empirical selection [52]. The choice of these parameters has been made during preliminary studies on their influence on the inversion result. Herein, the default values of the used open-source software package "inspyred" [53] resulted in a good balance between localizing the minimum and rapid convergence of the swarm, minimizing the total run-time of our problem. The "inertia" was, hereby, $w = 0.5$ to enable an equal weight between the past and the current information, and the scaling factors were $c_1 = c_2 = 2.1$. These values fall within a range of values explored in previous works [54], [55]. The "neighborhood size" was set to the entire population to ensure that the global best particle is considered when updating the velocity [49], [50].

## III. Antenna Model and Optimization Setup

### A. Experimental Reference Data

For the reference measurements in air, a metal plate was positioned 2 m ($3.3\,\lambda_{air}$) away from the antenna in order for the crosstalk and reflection to not overlap in time. The antenna was placed upside-down on the ground, covered by a 2 m layer of styrofoam and the metal plate centrally positioned on top of the styrofoam (see Fig. 1). This setup ensured that any spurious reflections from the ground or from nearby objects were minimized. Styrofoam was used because it provides an ideal balance between mechanical stability and having no effective influence on the signal. The material is nonmagnetic

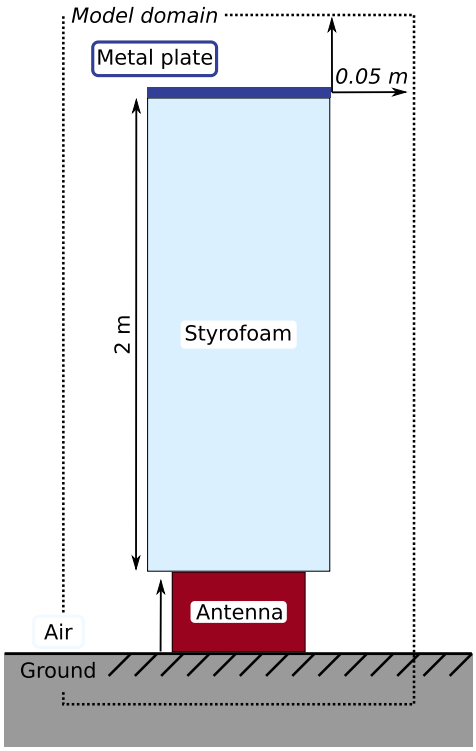


Fig. 1. Sketch of the measurement setup for gathering the reference data. The antenna is placed upside-down on the ground (i.e., with the dipoles at the top of the housing) with a 2 m layer of styrofoam and the metal plate (0.4 m × 0.4 m) on top. Indicated with a dashed border is the numerical model domain used for simulating the synthetic data.

and has a relative permittivity negligibly different to that of air [56]. To keep the simulation times as short as possible during the optimization, the metal plate needs to be small enough to fit inside a small model space but large enough to produce a strong enough reflection. A metal plate of 0.4 m × 0.4 m fulfilled both requirements. A dc-shift removal has been applied to center the amplitudes around zero, but no additional processing has been applied to the reference data. The full time signal, containing the crosstalk and reflected signal, is shown in Fig. 2.

### B. Design of the Antenna Model Geometry

The numerical 3-D model of the 400 MHz antenna (see Fig. 3) was created by first implementing the geometry of the real antenna, including the shape of the bowties, printing boards, absorber foam, metallic casing, plastic casing, and air gaps between particular materials. The real antenna includes a skid plate underneath the plastic casing. As both materials are made of plastic, we merged the skid plate and the plastic casing, resulting in an 8 mm-thick layer of plastic below the antenna bowties. Although the absorbing foam is probably composed of several different layers, we assumed a homogeneous absorber to reduce the number of fitting parameters. The transmission lines and electronic components were replaced with electric resistances on the transmitter and receiver feed edges. The resolution of the FD grid was set to 2 mm, which is a tradeoff between the need for high resolution

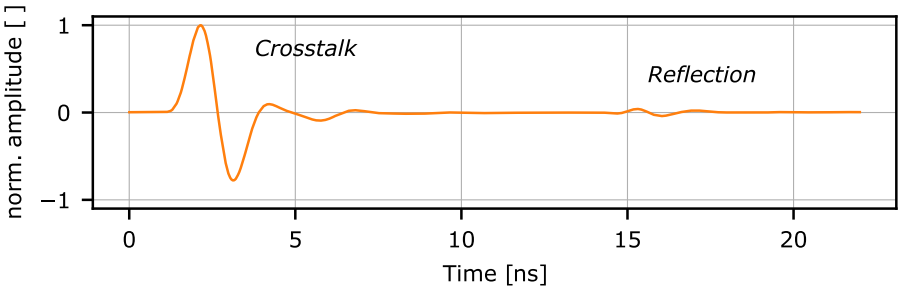


Fig. 2. Experimental reference signal of the 400 MHz antenna operated in air, containing the crosstalk at approx. 2 ns and the reflection of a metal plate at 2 m distance appearing at approx. 15 ns.

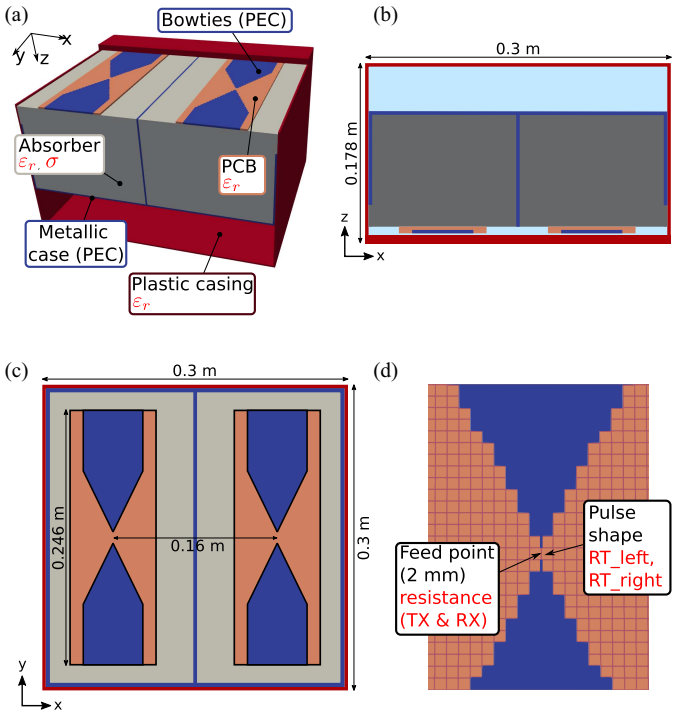


Fig. 3. (a) Upside-down view of the 3-D FDTD model of a 400 MHz GPR antenna, which has partly been opened for illustration of the inner components. Note that the bowties normally face downward toward the ground/medium. The abbreviated labels in the figure stand for the printed circuit board (PCB) and perfect electric conductor (PEC). The material parameters and labels in red are in the list of optimized parameters (I). (b) View and geometry of the $XZ$ plane through the middle of the antenna. (c) View and geometry of the plane on which the bowties lie. The dipole length of 0.246 m corresponds to $0.41\,\lambda_{air}$, while the antenna separation of 0.16 m corresponds to $0.26\,\lambda_{air}$. (d) Detailed view of the feed point of one of the bowties. The source/receiver points are the edges between the two PEC wires that extend from the bowties.

of the fine structures of the bowties and the computational capacities needed for a 3-D-simulation.

The feed point of the transmitter antenna is implemented by applying a voltage source between two conducting wires, i.e., over an FD grid edge, which connects to the bowties [see Fig. 3(d)]. The receiver point at the receiving antenna functions in the opposite way in which it records the voltage over that edge element. Furthermore, both feed points are assigned an electrical resistance, which is not the intrinsic antenna impedance at the open feed point a substitute of the characteristic feed line electrical resistance, balun, transmitter and receiver electronics, and so on, which are not included in the model.

### C. Optimization of the Antenna Material Parameters

Besides the transmitter and receiver electrical resistances on the feed points, the materials that compose the antenna were each assigned an electric conductivity $\sigma$ and a relative permittivity $\varepsilon_r$ in gprMax. We assumed the magnetic permeability of every material to be $\mu_r = 1$. We also assumed every material to have $\sigma = 0$, except for the absorbing foam. Exact values for the $\varepsilon_r$ and $\sigma$ of the absorbing foam, the $\varepsilon_r$ of the PCB, and the $\varepsilon_r$ of the plastic casing were unknown. Furthermore, it is common for the feed pulses of GPR antennas to be asymmetric [57], which is why we chose to construct a pulse that is made up of two differently steep Gaussian-shaped flanks. These two pulse flanks, as well as the abovementioned six parameter values, were the subject of the PSO optimization.

FDTD simulations of the same scenario as during the experiment were performed within the PSO optimization sequence. The model had the dimensions $0.5\ \text{m} \times 0.5\ \text{m} \times 2.26\ \text{m}$ [x, y, z]. For the simulation, the antenna was placed in the air ($\varepsilon_r = 1$), 2 m away from the metal plate, which was implemented as a PEC. Air was used as a substitute for the styrofoam in the experimental setup (see Fig. 1), as their relative permittivities are very similar. PMLs were placed at each border, with the default width of ten grid cells, to terminate the inbounding EM waves. The time discretization is determined by gprMax, in accordance to the Courant–Friedrichs–Lewy (CFL) condition [58] and with respect to the highest $\varepsilon_r$ in the model. The simulation time was set to 24 ns to ensure that the reflected wavelet and its coda are completely recorded.

The calculation of the rel. RMSE corresponding to each particle, i.e., a particular set of material parameter values, begins with cutting out and isolating the reflected signals in the reference and simulated traces. They are then each resampled at the same rate of $1 \cdot 10^{-3}$ ns and normalized to their maximum absolute amplitude. The normalization is necessary because the GPR system records noncalibrated voltages, and therefore, the measured and simulated traces cannot be compared directly. Finally, the measured and simulated traces are stepwise shifted on to another in time until a minimum rel. RMSE is reached. The shift has to be performed to compensate for small geometry inaccuracies between the experimental setup and the numerical model. Furthermore, varying the antenna parameters during the optimization causes changes of time zero, when the signal is emitted by the

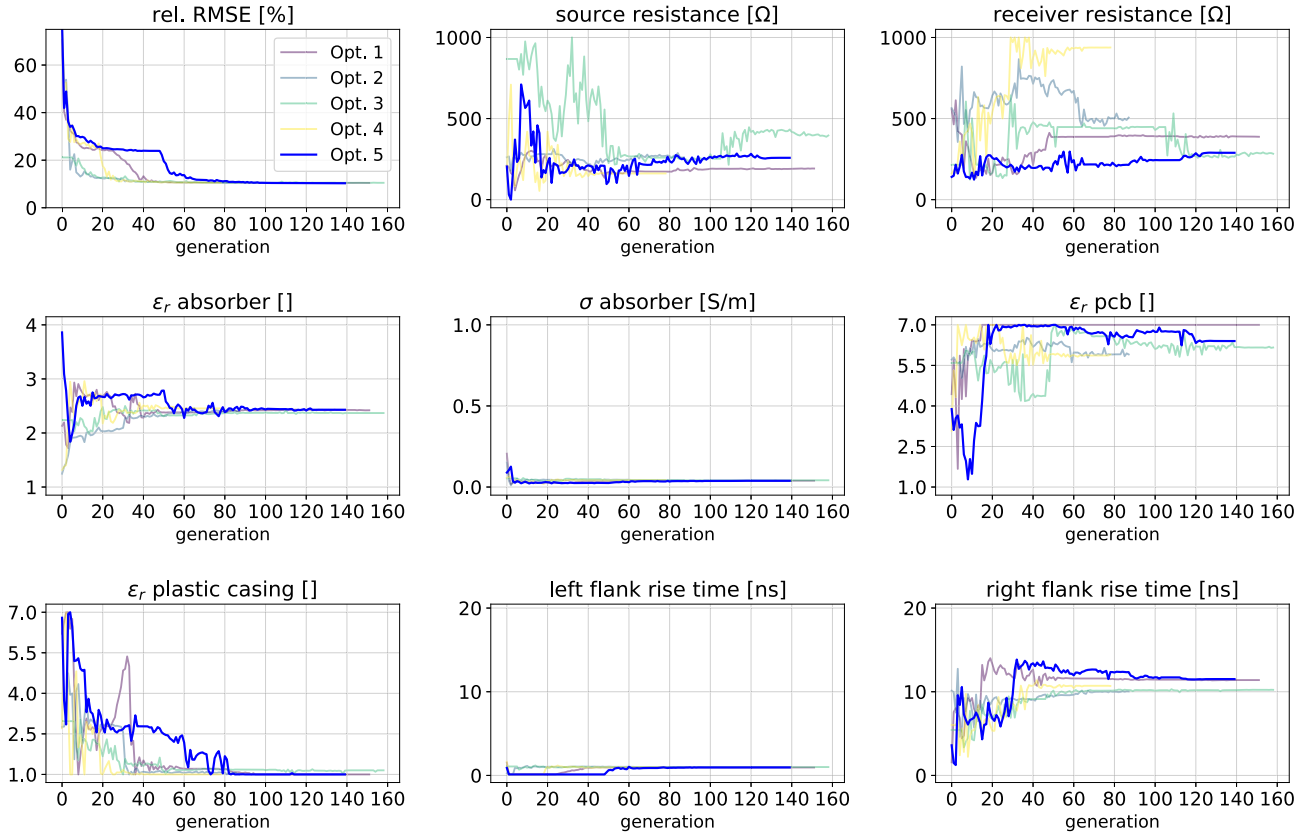


Fig. 4. Progression of the PSO optimization for the best five runs. The best particle of the swarm within each generation is plotted with its rel. RMSE values and corresponding antenna parameters. The blue curve shows the optimization with the best, final overall rel. RMSE. In the top left diagram, the upper rel. RMSE-limit is lower than the maximum value (189%) to be able to observe more details of the progression.

antenna. The resulting, minimum rel. RMSE value is then assigned to each particle.

The lower bounds of the electrical resistances were set to 0.01 Ω because a value of zero would produce a hard source in the FDTD algorithm that causes unwanted reflections from inbounding EM field variations. The upper bounds were set to a high value of 1000 Ω. The bounds of the absorber $\varepsilon_r$ were set to the natural lower limit of one and an upper limit of four, as the absorber is typically a foam, which mostly consists of air and, hence, has a low permittivity. The electrical conductivity of the absorber was also unknown, and we chose to use a range from 0 to 1 S/m. The latter value corresponds to very high attenuation of ≈337 dB/m for $\varepsilon_r = 2$ with a center frequency of 400 MHz. For a two-way travel path of approximately 0.4 m within the antenna case, this produces an amplitude attenuation of ≈135 dB, which is higher than the dynamic range of the GPR system. The bounds for the $\varepsilon_r$ of the PCB and plastic casing were also set to the natural lower limit of one and an upper limit of seven. The latter represents a high value for typical PCB material, e.g., FSR-4, as well as for a common plastic, e.g., high-density polyethylene [59], [60].

The two pulse flanks were each assigned a rise time (RT), which is the time the pulse rises from quasi-zero to maximum amplitude ($RT_{left}$) or falls from maximum amplitude to zero ($RT_{right}$), respectively. As a Gaussian function approaches zero asymptotically, we used a lower threshold of 1.11% of the maximum value to define the beginning of the RTs, which corresponds to three times the standard deviation of a normal Gaussian function. When $t_{max}$ is the time of maximum feed-pulse amplitude, we get

$$f(t) = \begin{cases} e^{-\frac{1}{2}\left(\frac{3(t-t_{max})}{RT_{left}}\right)^2}, & \text{for } t \leq t_{max} \\ e^{-\frac{1}{2}\left(\frac{3(t-t_{max})}{RT_{right}}\right)^2}, & \text{for } t > t_{max}. \end{cases} \quad (4)$$

The two RTs had lower and upper limits of 0.12 and 19.5 ns. Low RTs create very steep flanks with a higher frequency content than high RTs. The value 0.12 ns was the lowest possible to implement in the simulation due to the CFL criterion. However, such a pulse rise is much steeper than the one that can typically be realized in the electronics of GPR transmitters. A feed signal with an RT larger than $2 \cdot 19.5$ ns results in the signal energy only barely having entered the simulation at all and produces strong variations in the crosstalk and the transmitted signal. Furthermore, pulses with such long RTs contain very little to no energy around the center frequency of a 400 MHz antenna and would, therefore, not be suited to drive the antenna effectively (see Fig. 6). An overview of the parameter bounds is summarized in Table I, together with the final optimized parameter values.

For the optimization of the eight antenna parameters, the PSO algorithm was set up with a population of 40 particles. We found this number to be a good compromise between the total run-time per generation and sampling the 8-D parameter space. A single FDTD forward simulation runs in approx.

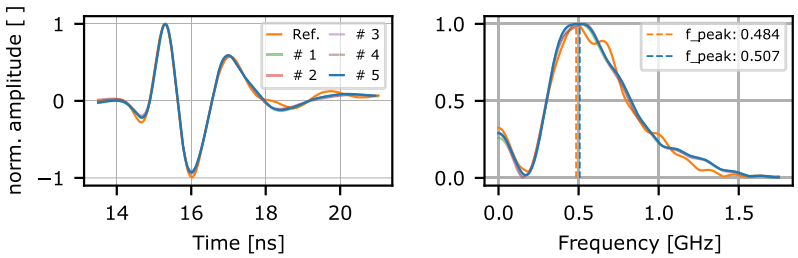


Fig. 5. Experimental reference signal and fit model responses: reflections from metal plates in air, produced by the best antenna models from each of the best five optimization runs (see Fig. 4). The orange curve is the measured, reference data, and the blue curve results from the overall best antenna model. Only the peak frequency of the reference data and the overall best, #5 (blue) are specified on the right-hand side.

2 min, resulting in ≈1.5 h. computation time per generation. The parameter space is, thereby, only sparsely sampled but, even increasing the number of particles significantly, will only result in a marginally better sampling of the individual parameter dimension, while the calculation time will dramatically increase. To counteract the relatively small number of particles per optimization, we ran ten optimization processes with different seeds and analyzed the spread of the results. This will provide a measure of the uncertainty of the parameters of the final antenna model.

We defined the stopping criterion for the optimization process by analyzing the long-term trend. This is because the rel. RMSE of a PSO optimization is not necessarily decreasing steadily but is prone to temporary fluctuations, e.g., when migrating from a local to a global minimum. Comparing the best rel. RMSE of the swarm of the current generation to that of ten generations prior proved to be a stable measure of the convergence. We stopped the optimization when the change of the best rel. RMSE in the aforementioned comparison was smaller than 0.01%.

## IV. Results

### A. Optimization Results and Analysis

Of the ten optimization runs launched with different seeds, five converged at rel. RMSE of ca. 10.5%, while the other five converged at ca. 20%. The latter would result in signal reflections that show significant differences to the measured curves. For the best five optimization runs, the optimization progression of the rel. RMSE values of the best particle per generation is shown in Fig. 4. All parameters converge within the given search interval, with the exception of the $\varepsilon_r$ casing, which converges very gradually to the lower limit of one. For the aforementioned five best optimization runs, the simulated reflections of the best antenna models, as well as the reference data, are shown in Fig. 5.

Optimization run #5 contains the particle, i.e., set of antenna model properties with the lowest final rel. RMSE of 10.3%. The other four optimization runs have similarly low, final rel. RMSE values, and their reflected signals are barely visually discernable. The final antenna model produces a reflection from a metal plate in the air that very accurately fits to the measured trace in terms of the amplitudes and zero-crossings (see Fig. 5). Also, the frequency spectrum of the reflected wavelet is very well reproduced by the antenna model. It is noteworthy that, for comparison, all data curves in the time domain are shifted to the point of minimum misfit,

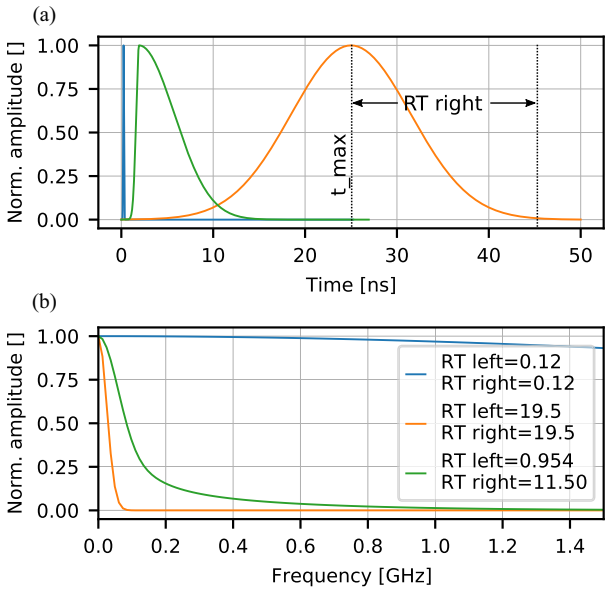


Fig. 6. (a) Source pulse shapes and (b) amplitude spectrum illustrating the full range of RTs used for the optimization. The sharpest possible pulse (blue), the smoothest possible pulse (orange), and the optimization result (green). The orange curve includes a visual representation of $RT_{right}$. The RTs are in ns.

a process that is repeated for all data curves in the time domain from hereon.

Table I summarizes the optimized antenna parameters, including the value of the best PSO inversion run (optimized value), the bounds of the search range, and the spread of the results of the best five inversion runs. These resulted in similarly good results with a misfit between 10.3% and 10.5%.

The pulse form that is produced by the final $RT_{left}$ and $RT_{right}$ values is plotted in Fig. 6. Therein also depicted for comparison are the sharpest and smoothest pulses that are produced by the parameter bounds.

In Fig. 7, we show all particles of all ten optimization runs, thus regardless of the generation, per pair of parameters. This provides a visualization of the fitness function within the search range of the PSO. One has to note that this figure shows the projection of an 8-D parameter space on the plane of the depicted pair of two parameters. The data were plotted in order of decreasing rel. RMSE, i.e., the good antenna models are plotted on top and hide less good parameter combinations that lie behind them. We can, thereby, see the overall distribution of particles with low rel. RMSE in terms of the space that each parameter pair encompasses. Relative RMSE values above 16% (the maximum is 189%) are

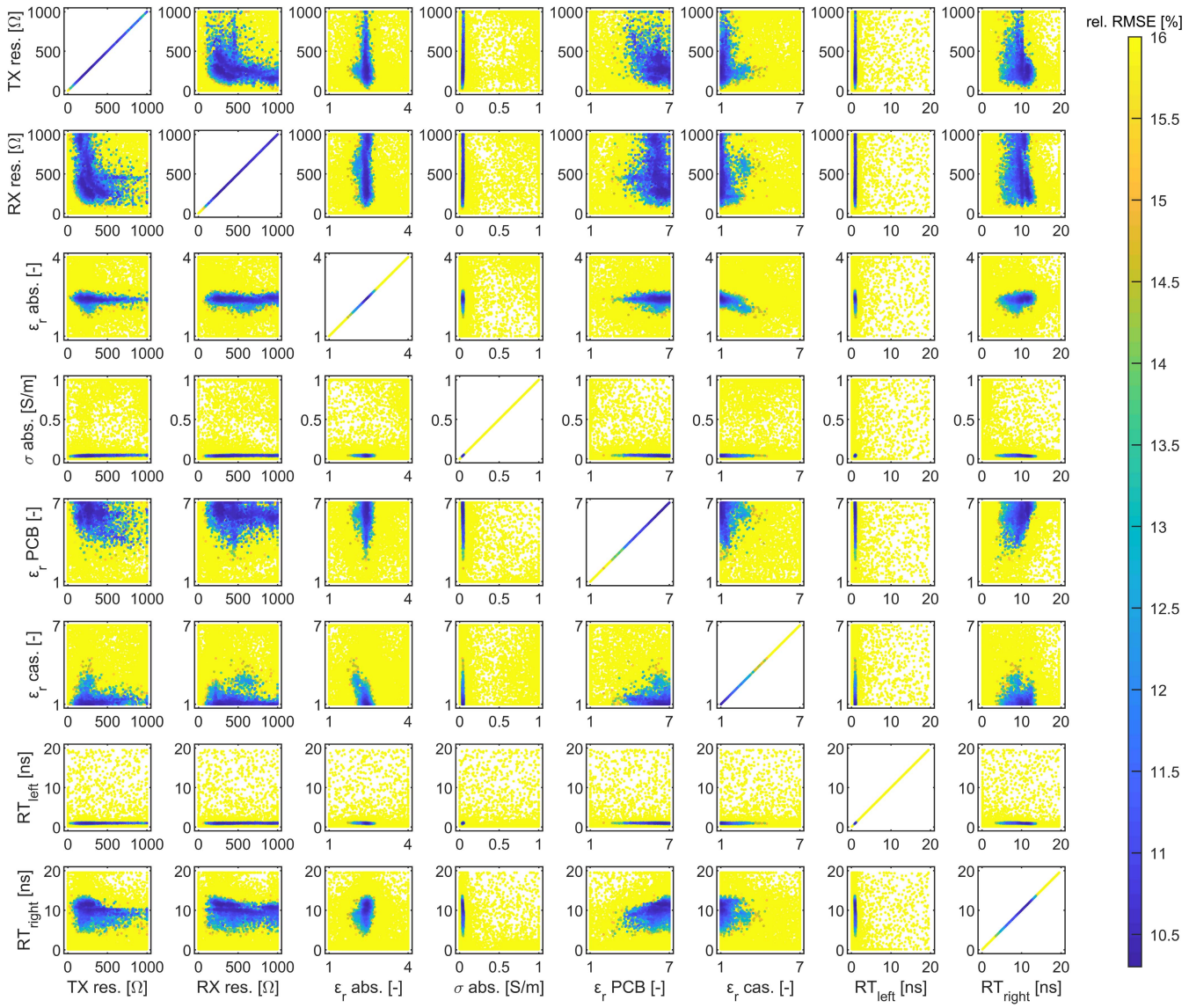


Fig. 7. Scatterplot of every pairwise combination of fitting parameters of all particles and generations for all ten optimization runs and corresponding misfits.

plotted in yellow and not differentiated in the colorbar because such antenna models generated signals that show noticeable differences to the measured signal in terms of amplitude and zero-crossings. Particles with hues of blue exhibit the best fits with little to no visual differences between each other and the reference trace. It is obvious that, for some antenna parameters as, e.g., the absorber conductivity and $RT_{left}$, the minimum of the rel. RMSE is sharp, which means that the fitness function is very sensitive to this parameter. On the other hand, the fitness function is less sensitive to, e.g., the source and receiver electrical resistances or $RT_{right}$, which both exhibit a rather broad minimum plateau. We can also see some dependencies between individual antenna parameters. For instance, the rel. RMSE is small if either one or both source or receiver electrical resistances are at around 250 Ω, but the rel. RMSE is high, if both electrical resistances are high.

Fig. 7 gives a rather general overview of the sensitivity of the fitness function to the individual parameters. A more detailed insight into the vicinity of the minima is given in Fig. 8, which shows the sensitivity of the rel. RMSE to a single parameter when the other parameters are kept constant at their optimum value. To clarify, the overall 8-D parameter-space may look more complex. The changes to single parameters are, therefore, dependent on the remaining parameter values that are taken from the final antenna model. The rel. RMSE range is limited to 100% and does not show the maximum values to gain more visible information in the range of "good" fits. We can see that the source and receiver electrical resistances have the lowest impact on the emitted wavelet shape, where the impact of $\sigma$ absorber and $RT_{right}$ is very strong, with a very sharp and pronounced minimum of the fitness function.

### *B. Validation of the Optimized Antenna Model*

In this section, the final antenna model obtained from the parameter optimization (see Table I) is validated for different scenarios. We show the comparison of simulations and measurements for the crosstalk and the amplitude ratio between crosstalk and reflection with the antenna operated in air, the

TABLE I

PARAMETERS (SEE ANTENNA MODEL IN FIG. 3), THEIR RESP. BOUNDS, OPTIMIZED VALUES, AND THE RANGE OF OPTIMIZED VALUES FOUND BY THE BEST FIVE OPTIMIZATION RUNS. THE OPTIMIZED VALUES FOR THE ANTENNA MODEL PRODUCED A SIGNAL WITH A REL. RMSE OF 10.3%

| Parameter | lower bound | upper bound | optimized value | range of results | | |
|---|---|---|---|---|---|---|
| TX resistance [Ω] | 0.01 | 1000 | 257.97 | 161 | – | 398.96 |
| RX resistance [Ω] | 0.01 | 1000 | 288.93 | 287.18 | – | 938.12 |
| $\varepsilon_r$ absorber [ ] | 1 | 4 | 2.43 | 2.37 | – | 2.46 |
| $\sigma$ absorber [S/m] | 0 | 1 | 0.0383 | 0.0377 | – | 0.0418 |
| $\varepsilon_r$ PCB [ ] | 1 | 7 | 6.40 | 5.83 | – | 7 |
| $\varepsilon_r$ casing [ ] | 1 | 7 | 1.00 | 1 | – | 1.15 |
| $\mathrm{RT}_{\mathrm{left}}$ [ns] | 0.12 | 19.5 | 0.954 | 0.942 | – | 1.01 |
| $\mathrm{RT}_{\mathrm{right}}$ [ns] | 0.12 | 19.5 | 11.5 | 10.1 | – | 11.5 |

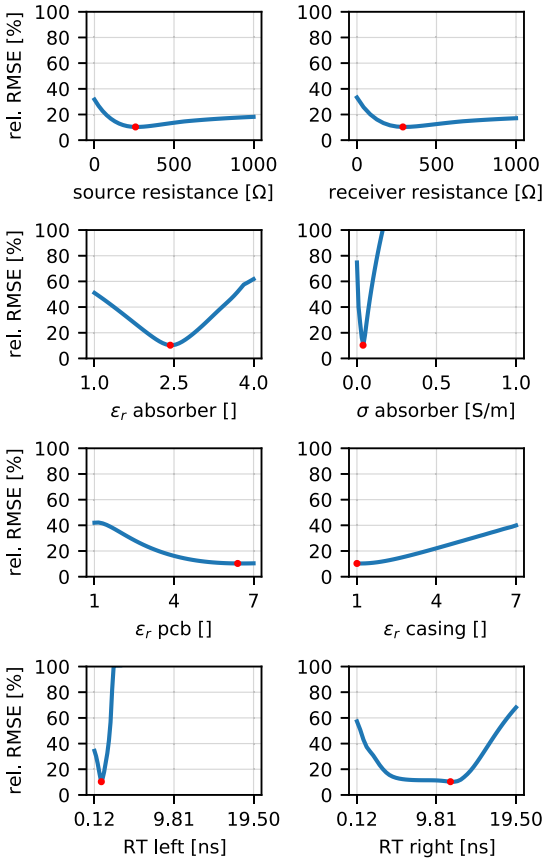


Fig. 8. Sensitivity study in the 1-D space of every fitting parameter for the final antenna model. The values for the remaining parameters are held constant at the optimized value, i.e., minimal rel. RMSE (red points).

antenna operated on water, and the signal caused by a metal plate in the near field of the antenna. A good fit of simulated and experimental data for this broadband of scenarios is a good indication that the antenna model produces accurate results, regardless of the medium in use.

*Crosstalk and Amplitude Ratio Reflection/Crosstalk*

As we only used the signal reflected at a metal plate in the air for optimizing the antenna parameters, the antenna crosstalk is an independent property that can be used to validate the model. The peak-to-peak amplitudes and zero-crossings conform very well to the measured data, and there are only small-signal deviations in the coda, between 3.75 and 8 ns (see Fig. 9). There is also a good fit in the amplitude spectra of both curves, and the observation that the crosstalk of the antenna has a lower frequency than the emitted wavelet is well reproduced by the model. The amplitude ratio of a reflection to that of the antenna crosstalk is a characteristic of the distance of the reflecting object, its radar cross section, and the antenna characteristics. The amplitude ratio in the measured trace is ≈0.0408, and that of the simulated trace is ≈0.0389, which corresponds to a deviation of <5% and confirms the validity of the antenna model for applications in air.

*Antenna Operated on Water*

We tested the performance of the antenna model on water, which is an extreme case as water has the highest permittivity of all materials that have to be expected in the field. We compare the simulated and measured reflections from a metal plate (with the dimensions 0.3 m × 0.4 m) placed at 0.35 m depth in water ($3.2\,\lambda_{water}$), with the antenna resting on the water surface (see Fig. 10). The metal plate was connected to the antenna via nylon strings and positioned centrally below the antenna. In the simulation, the frequency-dependent complex dielectric properties of water are implemented via a Debye-pole, for which we obtained the temperature-dependent relaxation parameters provided by [61]. For a temperature of 15 °C, this resulted in a static relative permittivity of $\varepsilon_0 = 82.1$, the high-frequency relative permittivity of $\varepsilon_\infty = 6.0$, and the relaxation time of $\tau = 10.8 \cdot 10^{-3}$ ns. The dc conductivity of the water was measured with a conductometer to be $\sigma = 0.0259$ S/m and was directly implemented in the model. In Fig. 11, we can see that the reflection is very well simulated with only small amplitude variations in the coda and almost identical frequency spectrum and peak frequencies. However, the simulated antenna crosstalk does not fit as well, and there are significant differences in the peak-to-peak amplitude ratio and the zero crossings. Also, the amplitude ratio of crosstalk and reflected wave of the measured trace (≈5.85) is not reproduced accurately in the simulation (≈2.03). The peak frequency is emulated quite well even though the simulated trace contains higher frequencies than the measured one.

*Metal Plate Within the Near Field of the Antenna*

The calibration data were obtained with a metal plate at a 2 m distance to the antenna and characterize the emitted

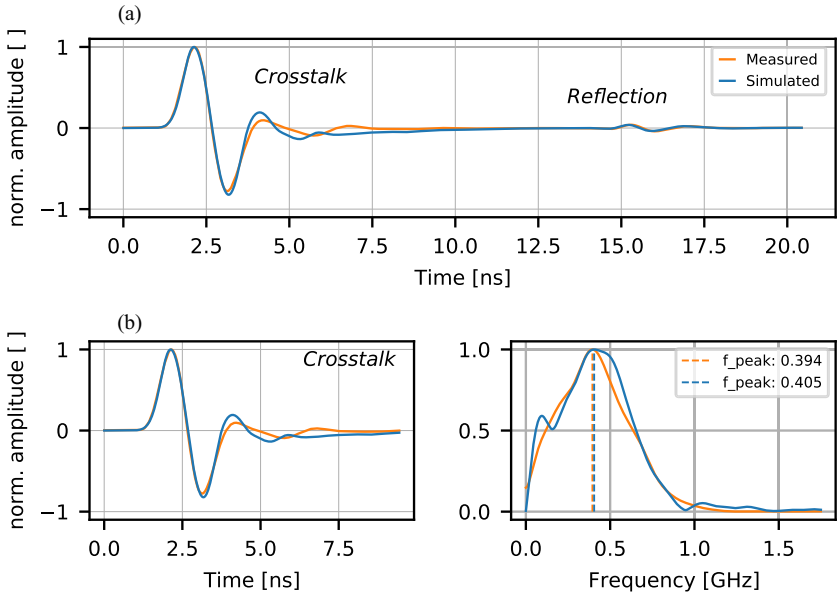


Fig. 9. Model validation: measured and simulated signal of the antenna operated in the air with a metal plate at 2 m distance. (a) Full trace containing the crosstalk and reflection from the metal plate. (b) Cut-out crosstalk; the left-hand side contains the signals in time, with the corresponding frequency spectra and peak frequencies to the right.

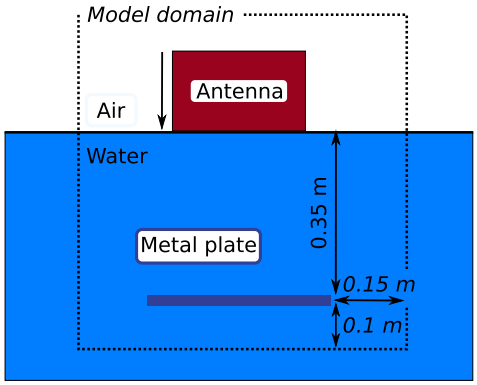


Fig. 10. Sketch of the measurement setup for the antenna validation in water. The antenna is placed on the water surface with normal orientation, i.e., the dipoles at the bottom of the housing. The metal plate (0.3 m × 0.4 m) is placed centrally 0.35 m below the antenna and held by four thin nylon strings. Indicated with a dashed border is the model domain for simulating the synthetic data.

wavelet. We performed three additional measurements with the metal plate in the reactive near field of the antenna and compared them to simulations with the optimized antenna model (see Fig. 12). The measurements were done at distances of 0 m, which corresponds to a capacitive short-circuiting of the antenna, 0.06 m ($0.1\,\lambda_{air}$) and 0.13 m ($0.22\,\lambda_{air}$). The resulting signals change strongly with varying distances of the metal plate to the antenna. This is due to a direct influence of the plate on the antenna's characteristics and interference patterns resulting from the signals bouncing between the plate and the antenna. The simulated and measured signals are very similar, with some small deviations in the peak-to-peak amplitude ratio, especially when the antenna is placed directly on the metal plate. At 0 m, there are also some small deviations of the zero-crossings, and the frequency spectrum of the simulated trace has a stronger low-frequency content. At 0.06 and 0.13 m, the overall shape, the zero-crossings, and the frequency spectra, with two notable peaks, fit well. The simulated traces have slightly higher peak frequencies than the measured traces but generally fit well.

## V. Discussion

This work builds upon the previous advances in antenna optimization, in particular by Warren and Giannopoulos [16] and Giannakis *et al.* [30]. There, GPR antennas with high center frequencies were optimized (1.2 and 1.5 GHz) by means of fitting the crosstalk of the antennas in air and the signal of an antenna terminated with a metal plate with a Taguchi and a hybrid linear/nonlinear FWI. In contrast, we optimized a lower frequency antenna and chose to fit the emitted wavelet rather than the near-field behavior, which we used as model validation. In further contrast, we chose to use the global optimization scheme PSO because, much more than the aforementioned methods in [16] and [30], it is better able to tackle and explore the unknown, potentially multimodal multidimensional solution space in our problem. Being insensitive to a lack of *a priori* information and to local minima, the swarm behavior of the method is better suited for exploring the entirety of the solution space and, thus, has a higher chance of finding a global optimal solution. Despite these advantages, the PSO brings along a higher computational cost; however, current computational capabilities allow the use of such expensive optimization strategies. In addition, the effort for this kind of optimization procedure is only necessary once, as a successfully optimized antenna model can subsequently be used indefinitely for simulating/inverting various GPR scenarios. It shall be mentioned that the usage of other methods, such as hybrid variants of PSO and gradient methods, could be explored in this scenario in the future and may be able to find good solutions faster. We opted

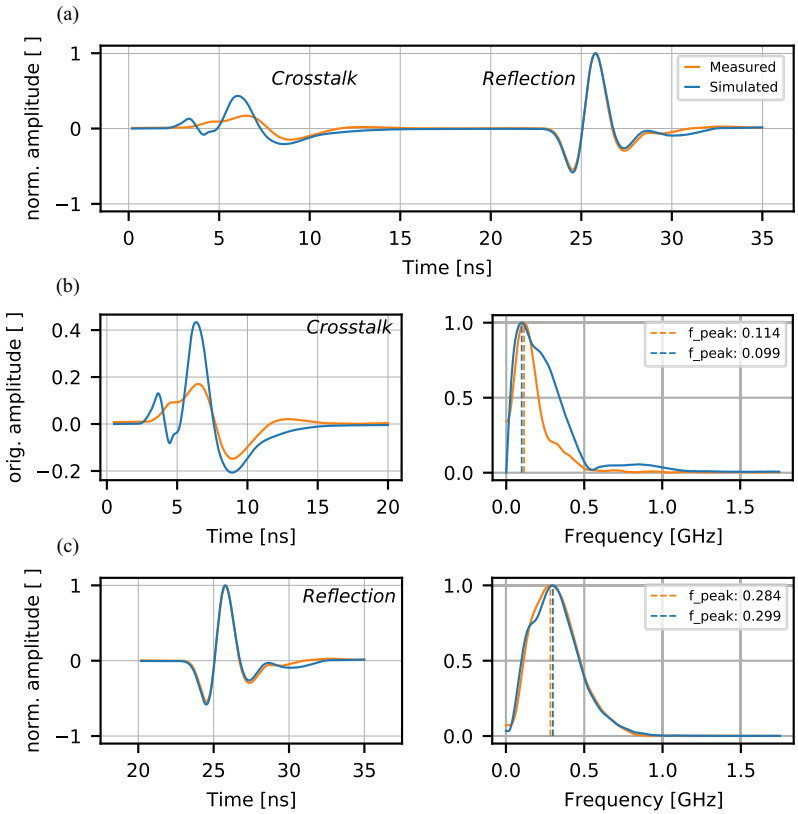


Fig. 11. Model validation: measured and simulated signal of the antenna operated on the water with a metal plate at 0.35 m distance. (a) Full trace containing the crosstalk and reflection from the metal plate. (b) Cut-out crosstalk. (c) Cut-out reflection. The left figures contain the signals in time, with the corresponding frequency spectra and peak frequencies on the right.

to use a PSO algorithm with multiple seeds due to the unpredictable and nonlinear influences of the parameters on the emitted wavelet. The results show that the similarly good, final optimized antenna models (see Fig. 5) do not strongly depend on the seed of the starting model as they almost all converge on similar values (see Fig. 4).

Creating an antenna model by fitting the parameters to calibration data will not necessarily result in an exact 1:1 replica of the real antenna but yields a model that shows a similar behavior and produces signals very close to that of the real antenna. Therefore, we did not expect that every parameter of the antenna model will converge to realistic values as a model simplification at one part of the antenna can cause a counterbalance in the properties of another part. In the end, our optimization routine yielded an antenna model that very accurately replicates measured signals in various scenarios. The model was validated in air and water, which covers the span of most extreme cases that can be expected in the field. It is able to replicate main aspects such as frequency shifts of the emitted wavelet when the antenna is operated on different media, the amplitudes, and zero-crossings of the signals, as well as near-field effects, such as interference patterns between crosstalk and reflected signals, multiple reflections, and antenna ringing.

### A. Experimental Limitations

As the calibration data are the basis of the deduced antenna model, the reproducibility of the experimental data was striven for but is variable for a number of reasons. First, measurements with different GPR antennas but of the same type probably produce slightly different signals caused by, e.g., manufacturing tolerances of the electronic components. Second, some experimental uncertainties remain even though much care was taken to accurately set up the geometries, avoid spurious reflections from the side and from improper lain cables, and minimize the time drift of the antenna and GPR apparatus. In summary, the experimental uncertainty is probably larger than the variance between the five best results of our PSO optimization runs that show a misfit between 10.3% and 10.5% to the calibration data. More accurate reference data from experiments under controlled conditions, e.g., in a box with varying homogeneous materials, would be desirable. However, realizing these measurements, with decreasing antenna frequencies and, consequently, rising wavelength and larger antennas, is costly and poses a big challenge.

### B. Model Limitations

All the geometric details that we could obtain were implemented in a numerical model (see Fig. 3) with a 2 mm spatial discretization, which could not be lowered due to the FDTD calculation capacities. Consequently, delicate structures as, e.g., the feed points of the bowties, PCB boards, or air gaps may not be resolved adequately. An improvement to these limiting circumstances would be to incorporate subgridding routines in the FDTD code in the future to be able to refine the model grid where the implementation of fine geometric

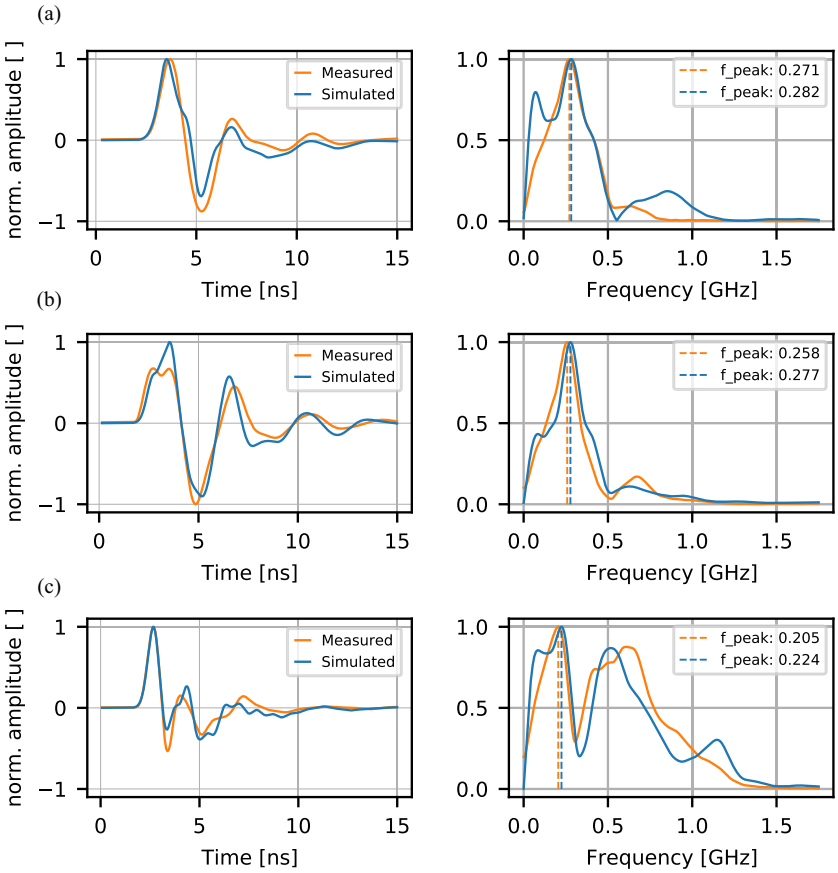


Fig. 12. Model validation: measured and simulated signal of antenna placed directly above a metal plate at distances of (a) 0, (b) 0.06, and (c) 0.13 m) in air. The left figures contain the signals in time, with the corresponding frequency spectra and peak frequencies to the right.

details is necessary while keeping the overall model size and simulation run-time at an acceptable level. Overall, not all antenna parts could be replicated completely and had to be either simplified, e.g., the absorber foam, or neglected, e.g., the transmitter and receiver electronics. Notably, the antenna electronics were implemented as transmitter and receiver resistances. Integrating the electronics of the antenna into the model and describing the interaction between electronics, transmission lines, and the antenna seem to be the most challenging point, and currently, there is no practicable solution in sight.

### C. Optimization Performance

Of the ten optimization runs that we started, and with our stopping criterion, five converged at rel. RMSE values of ≈10.5% (see Fig. 4). The "failure rate" of five out of ten optimizations converging at higher rel. RMSE values of ≈20% is most likely due to the entire parameter space being sparsely sampled and the complexity of the fitness function. These circumstances increase the probability of the PSO swarms converging in local minima. The simulated reflections of the best antenna models proved to have a very good fit to the measured trace with very little deviations in the amplitudes, zero-crossings, and frequency spectra (see Fig. 5).

The aforementioned five optimization runs show slightly different progressions. This was expected, as each optimization started with a different seed, and the total 8-D parameter space is large compared to the population size. Of the eight fit antenna parameters, the absorber conductivity and $RT_{left}$ proved to be well defined in all optimization runs and tended to have a large influence on the wavelet (see Figs. 4 and 7). The remaining six parameter are also found by all optimization runs ( see Table I), albeit at slightly different stages (see Fig. 4), which means that these parameters have a smaller influence on the wavelet.

### D. Fit Antenna Parameters

Even though the absorber was implemented with only one layer, as supposed to be several layers in the real antenna, its material components converged on nearly identical values in the five best optimization runs. Figs. 4 and 8 both show, that for $\varepsilon_r$ and especially $\sigma$ absorber, similar values are found fast, and they lie within a relatively well-defined minimum with regard to the rel. RMSE

The two RT parameters, of the left- and right-hand sides of feed pulse, are assigned two very different values, with a sharp rise from the start and a relatively slow decline after the maximum amplitude (see Fig. 6). Not only was a difference in the two parameters expected but also the sharp rise and slow fall in amplitude also coincide with the typical form of antenna feed pulses [57]. In all five optimizations, $RT_{left}$ converges on

almost the same value, while $RT_{right}$ shows some variation (see Table I).

The rel. RMSE as a function of $RT_{right}$ shows a rather broad minimum plateau (see Fig. 8), which indicates that it only has a small impact on the wavelet. In the future, the pulse form could be created in a more flexible manner, by increasing the parameterization of the pulse, albeit with a higher parameter number and therewith the expense of a longer optimization duration.

The source electrical resistance and, especially, the receiver electrical resistance are the parameters with the widest range in their final values. This indicates that these two parameters have a relatively small influence on the shape of the transmitted antenna signal. The absolute amplitude of the recorded signal is also influenced by the electrical resistances. This, however, cannot be considered in the optimization, as the amplitude is measured on an arbitrary scale by the GPR system and not given in calibrated voltages. Hence, we had to normalize the experimental and simulated data during the optimization.

The permittivity of the plastic casing is the only parameter that converged on one of its bounds, the lower bound of $\varepsilon_r = 1$, which is a nonrealistic value for plastic. We attribute this to be possibly an effect of geometric discrepancies between the real and numerical antennas due to the limited spatial discretization. These discrepancies include the small air gap between bowties and plastic casing, and the grooves of the skid plate that were not implemented in the model. Fig. 8 also shows that the rel. RMSE, as a function of the $\varepsilon_r$ of the plastic casing, does not have a steep descent in the vicinity of the minimum. This indicates that a slight change in $\varepsilon_r$ value would only slightly change the performance of the antenna, which would, in turn, however, represent a more realistic $\varepsilon_r$. A possible solution for finding a realistic value for $\varepsilon_r$ of the casing could be to weigh the match to a measured signal in a media other than air into the fitness function. This, however, will remove the option of independent validation of the antenna model or require further measurements under controlled conditions, e.g., by using oil–water emulsions as in [16]. The latter seems unfeasible or at least extremely expensive when targeting the emitted wavelet for lower frequency antennas.

### E. Validation and Performance of the Antenna Model

The validation studies support the accuracy and versatility of the antenna model. In the analyzed scenarios, the simulated traces showed characteristics that are very similar to those of the measured traces (see Figs. 9–12). The shape of the crosstalk in the air is almost perfectly reproduced, and the amplitude ratio of the reflection to the crosstalk ends up being very close with a deviation of $<5\%$. A possible future improvement could be to include and weigh the amplitude ratio in the fitness function of the optimization. When the antenna is operated on water, the emitted wavelet is also accurately reproduced by the model, including the significant shift in the center frequency when operated in water ($\approx$300 MHz) and air ($\approx$500 MHz). Only the shape of the crosstalk of the antenna on water could not be simulated precisely. This could be caused by the unrealistic permittivity of the casing ($\varepsilon_r = 1$) of our model or further geometric inaccuracies of the model, as discussed above. In addition, water flowing between the plastic casing and the skid plate mounted directly below it could possibly change the crosstalk signal in the experiment. This effect is not reproduced in the simulation, as the skid plate is not separately included in the antenna model. Finally, the differences could be caused by the feed cables and antenna electronics, which are both not included in the model, but might cause effects when the antenna is operated on material, for which it has not been designed leading to a mismatch of impedances. In the future, to reduce the misfits caused by simulating antennas on subsurface media different from that used in the optimization, a joint optimization on multiple media could be employed. This, of course, will require further accurate experimental data and increase the computation time of the optimization.

Despite the aforementioned differences in the crosstalk shape, when the antenna is operated on water, its peak frequency and total length are well reproduced. As the latter defines the time window of the radar trace that is masked, and as the wave emitted in water is emulated correctly, we deem the limitation of the simulated crosstalk acceptable. The near-field effects of the antenna are very well reproduced by the model and show only very small differences. They can be explained by minimal deviations of the geometry, i.e., the distance of the metal plate to the bowties, as the measured signal is the result of a complex interference pattern of crosstalk and reflection in the near field of the antenna.

### F. Transferability of the Approach

Generally speaking, the presented optimization methodology could be applied to antennas of different center frequencies. For antennas with higher center frequencies, the main limitation would be the fine numerical spatial discretization that might be necessary to achieve an adequately accurate numerical antenna replica. This point might become less impairing in the future with the usage of subgridding. On the plus side, higher frequency antennas are smaller in size, resulting in an overall smaller numerical model. For antennas with lower center frequencies, the spatial discretization needs not be that fine; however, gaining high-quality reference data without any side reflections becomes more difficult.

## VI. Conclusion

Generating realistic FDTD antenna models can be done by implementing the geometry of the main antenna components and fitting the unknown material properties and feed pulse to experimental data. The approach of using a set of particle swarm optimizations coupled with an FDTD forward calculation proved to be effective. Even though the model does not include all details due to the limited spatial discretization or simplifications as replacing the electronics of the antenna with electrical resistance, all but one of the fit parameters were in the range of realistic values. Analyzing the fitness function, i.e., the misfit of the model response, provides an insight into the sensitivity of the signal of the antenna to the

single antenna components. The absorber properties and the feed pulse shape were the most influencing factors, whereas the other material properties and the electrical resistance of the electronics proved to be less important. The final optimized model is able to reproduce the main features of the antenna very precisely. This includes frequency shifts of the emitted wavelet, when subsurface properties change, and complex interference patterns, when an object is placed in the near field of the antenna. Including full antenna models and accounting for the described effects are, therefore, superior to using simple dipole point sources and crucial for realistic simulations used for, e.g., FWI. The presented 400 MHz model is a replica of an antenna that is widely used in geoscientific and engineering applications, and can directly be used by the GPR community. Further antenna models can be designed by following the presented optimization approach and incorporating the required unknown parameters of that particular antenna. Besides information on the geometry of the major components of the antenna, it would be helpful if calibration data of antennas on different materials were available, e.g., by the manufacturers. These data could form the basis to build up an open-source antenna model database, from which the whole GPR community will benefit.

## Data and Materials Availability

Data associated with this research are available and can be accessed via the DOI 10.5281/zenodo.4740601. We intend to provide the antenna model to the community via the open-source software platform of gprMax.

## Acknowledgment

The authors thank Stephan Schennen and Thomas Hiller for internal review. They also sincerely thank the two anonymous reviewers for their constructive criticism that contributed to the improvement of this article.

## References

[1] D. K. Butler, *Near-Surface Geophysics*. Tulsa, OK, USA: SEG, Jan. 2005, doi: 10.1190/1.9781560801719.

[2] H. Jol, *Ground Penetrating Radar: Theory and Applications*. Amsterdam, The Netherlands: Elsevier, Jan. 2009.

[3] L. Gurel and U. Oguz, "Optimization of the transmitter-receiver separation in the ground-penetrating radar," *IEEE Trans. Antennas Propag.*, vol. 51, no. 3, pp. 362–370, Mar. 2003, doi: 10.1109/TAP.2003.809873.

[4] N. Allroggen and J. Tronicke, "Attribute-based analysis of time-lapse ground-penetrating radar data," *Geophysics*, vol. 81, no. 1, pp. H1–H8, Jan. 2016, doi: 10.1190/geo2015-0171.1.

[5] J. van der Kruk, N. Diamanti, A. Giannopoulos, and H. Vereecken, "Inversion of dispersive GPR pulse propagation in waveguides with heterogeneities and rough and dipping interfaces," *J. Appl. Geophys.*, vol. 81, pp. 88–96, Jun. 2012, doi: 10.1016/j.jappgeo.2011.09.013.

[6] P. Koyan and J. Tronicke, "3D modeling of ground-penetrating radar data across a realistic sedimentary model," *Comput. Geosci.*, vol. 137, Apr. 2020, Art. no. 104422, doi: 10.1016/j.cageo.2020.104422.

[7] L. Liu, Z. Li, S. Arcone, L. Fu, and Q. Huang, "Radar wave scattering loss in a densely packed discrete random medium: Numerical modeling of a box-of-boulders experiment in the Mie regime," *J. Appl. Geophys.*, vol. 99, pp. 68–75, Dec. 2013, doi: 10.1016/j.jappgeo.2013.08.022.

[8] I. Giannakis, A. Giannopoulos, and C. Warren, "A realistic FDTD numerical modeling framework of ground penetrating radar for landmine detection," *IEEE J. Sel. Topics Appl. Earth Observ. Remote Sens.*, vol. 9, no. 1, pp. 37–51, Jan. 2016, doi: 10.1109/JSTARS.2015.2468597.

[9] M. Loewer and J. Igel, "FDTD simulation of GPR with a realistic multi-pole Debye description of lossy and dispersive media," in *Proc. 16th Int. Conf. Ground Penetrating Radar (GPR)*, Jun. 2016, pp. 1–5, doi: 10.1109/icgpr.2016.7572599.

[10] A. Klotzsche, H. Vereecken, and J. van der Kruk, "Review of crosshole ground-penetrating radar full-waveform inversion of experimental data: Recent developments, challenges, and pitfalls," *Geophysics*, vol. 84, no. 6, pp. H13–H28, Nov. 2019, doi: 10.1190/geo2018-0597.1.

[11] A. Taflove and S. Hagness, *Computational Electromagnetics: The Finite-Difference Time-Domain Method* (Artech House Antennas and Propagation Library). Norwood, MA, USA: Artech House, 2005.

[12] N. J. Cassidy, "A review of practical numerical modelling methods for the advanced interpretation of ground-penetrating radar in near-surface environments," *Near Surf. Geophys.*, vol. 5, no. 1, pp. 5–21, Sep. 2006, doi: 10.3997/1873-0604.2006014.

[13] K. Yee, "Numerical solution of initial boundary value problems involving Maxwell's equations in isotropic media," *IEEE Trans. Antennas Propag.*, vol. AP-14, no. 3, pp. 302–307, May 1966, doi: 10.1109/TAP.1966.1138693.

[14] C. Balanis, *Antenna Theory: Analysis and Design*. Hoboken, NJ, USA: Wiley, 2016.

[15] D. Caratelli, A. Yarovoy, and L. Ligthart, "Accurate FDTD modelling of resistively-loaded bow-tie antennas for GPR applications," in *Proc. 3rd Eur. Conf. Antennas Propag.*, Berlin, Germany, Apr. 2009, pp. 2115–2118.

[16] C. Warren and A. Giannopoulos, "Creating finite-difference time-domain models of commercial ground-penetrating radar antennas using Taguchi's optimization method," *Geophysics*, vol. 76, no. 2, pp. G37–G47, Mar. 2011, doi: 10.1190/1.3548506.

[17] K.-H. Lee, C.-C. Chen, F. L. Teixeira, and R. Lee, "Modeling and investigation of a geometrically complex UWB GPR antenna using FDTD," *IEEE Trans. Antennas Propag.*, vol. 52, no. 8, pp. 1983–1991, Aug. 2004, doi: 10.1109/TAP.2004.832501.

[18] N. Diamanti, J. Redman, and A. Annan, "Importance of simulating realistic transducers in GPR numerical modelling," in *Proc. Near Surf. Geosci., 20th Eur. Meeting Environ. Eng. Geophys.* Utrecht, The Netherlands: EAGE Publications, Sep. 2014, pp. 1–5, doi: 10.3997/2214-4609.20142097.

[19] C. S. Bristow and H. M. Jol, *Ground Penetrating Radar in Sediments*, vol. 211, no. 1. London, U.K.: Geol. Soc. London, Jan. 2003.

[20] A. P. Annan, *Near-Surface Geophysics*. Tulsa, OK, USA: SEG, Jan. 2005, ch. 11, pp. 357–438, doi: 10.1190/1.9781560801719.

[21] M. Salucci, G. Oliveri, and A. Massa, "GPR prospecting through an inverse-scattering frequency-hopping multifocusing approach," *IEEE Trans. Geosci. Remote Sens.*, vol. 53, no. 12, pp. 6573–6592, Dec. 2015, doi: 10.1109/TGRS.2015.2444391.

[22] A. Fedeli, M. Pastorino, and A. Randazzo, "Advanced inversion techniques for ground penetrating radar," *J. Telecommun. Inf. Technol.*, vol. 3, pp. 37–42, Jan. 2017, doi: 10.26636/jtit.2017.119717.

[23] J. M. Bourgeois and G. S. Smith, "A fully three-dimensional simulation of a ground-penetrating radar: FDTD theory compared with experiment," *IEEE Trans. Geosci. Remote Sens.*, vol. 34, no. 1, pp. 36–44, Jan. 1996, doi: 10.1109/36.481890.

[24] J. M. Bourgeois and G. S. Smith, "A complete electromagnetic simulation of a ground penetrating radar for mine detection: Theory and experiment," in *IEEE Antennas Propag. Soc. Int. Symp. Dig.*, vol. 2, Jul. 1997, pp. 986–989, doi: 10.1109/APS.1997.631693.

[25] R. L. Roberts and J. J. Daniels, "Modeling near-field GPR in three dimensions using the FDTD method," *Geophysics*, vol. 62, no. 4, pp. 1114–1126, Jul. 1997, doi: 10.1190/1.1444212.

[26] K. Holliger and T. Bergmann, "Accurate and efficient FDTD modeling of ground-penetrating radar antenna radiation," *Geophys. Res. Lett.*, vol. 25, no. 20, pp. 3883–3886, Oct. 1998, doi: 10.1029/1998GL900049.

[27] B. Lampe, K. Holliger, and A. G. Green, "A finite-difference time-domain simulation tool for ground-penetrating radar antennas," *Geophysics*, vol. 68, no. 3, pp. 971–987, May 2003, doi: 10.1190/1.1581069.

[28] C. Warren and A. Giannopoulos, "Characterisation of a ground penetrating radar antenna in lossless homogeneous and lossy heterogeneous environments," *Signal Process.*, vol. 132, pp. 221–226, Mar. 2017, doi: 10.1016/j.sigpro.2016.04.010.

[29] S. Stadler and J. Igel, "A numerical study on using guided GPR waves along metallic cylinders in boreholes for permittivity sounding," in *Proc. 17th Int. Conf. Ground Penetrating Radar (GPR)*, Jun. 2018, pp. 1–4, doi: 10.1109/icgpr.2018.8441666.

[30] I. Giannakis, A. Giannopoulos, and C. Warren, "Realistic FDTD GPR antenna models optimized using a novel linear/nonlinear full-waveform inversion," *IEEE Trans. Geosci. Remote Sens.*, vol. 57, no. 3, pp. 1768–1778, Mar. 2019, doi: 10.1109/TGRS.2018.2869027.
[31] W.-C. Weng, F. Yang, and A. Elsherbeni, "Electromagnetics and antenna optimization using Taguchi's method," *Synth. Lectures Comput. Electromagn.*, vol. 2, no. 1, pp. 1–94, Jan. 2007, doi: 10.2200/S00083ED1V01Y200710CEM018.
[32] R. Poli, "Analysis of the publications on the applications of particle swarm optimisation," *J. Artif. Evol. Appl.*, vol. 2008, pp. 1–10, Jan. 2008, doi: 10.1155/2008/685175.
[33] J. L. Fernandez-Martinez, J. P. Fernández-Alvarez, M. E. García-Gonzalo, C. O. M. Pérez, and H. A. Kuzma, "Particle swarm optimization (PSO): A simple and powerful algorithm family for geophysical inversion," in *SEG Technical Program Expanded Abstracts*. Tulsa, OK, USA: SEG, Jan. 2008, doi: 10.1190/1.3064068.
[34] J. Stork, A. E. Eiben, and T. Bartz-Beielstein, "A new taxonomy of global optimization algorithms," *Natural Comput.*, pp. 1–24, Nov. 2020, doi: 10.1007/s11047-020-09820-4.
[35] R. Shaw and S. Srivastava, "Particle swarm optimization: A new tool to invert geophysical data," *Geophysics*, vol. 72, no. 2, pp. F75–F83, Mar. 2007, doi: 10.1190/1.2432481.
[36] F. A. Monteiro Santos, "Inversion of self-potential of idealized bodies' anomalies using particle swarm optimization," *Comput. Geosci.*, vol. 36, no. 9, pp. 1185–1190, Sep. 2010, doi: 10.1016/j.cageo.2010.01.011.
[37] F. Pace, A. Santilano, and A. Godio, "Particle swarm optimization of 2D magnetotelluric data," *Geophysics*, vol. 84, no. 3, pp. E125–E141, May 2019, doi: 10.1190/geo2018-0166.1.
[38] J. Tronicke, H. Paasche, and U. Boniger, "Join global inversion of GPR and P-wave seismic traveltimes using particle swarm optimization," in *Proc. 6th Int. Workshop Adv. Ground Penetrating Radar (IWAGPR)*, Jun. 2011, pp. 1–4, doi: 10.1109/iwagpr.2011.5963884.
[39] J. Tronicke, H. Paasche, and U. Böniger, "Crosshole traveltime tomography using particle swarm optimization: A near-surface field example," *Geophysics*, vol. 77, no. 1, pp. R19–R32, Jan. 2012, doi: 10.1190/geo2010-0411.1.
[40] G. Hamann and J. Tronicke, "Global inversion of GPR traveltimes to assess uncertainties in CMP velocity models," *Near Surf. Geophys.*, vol. 12, no. 4, pp. 505–514, Nov. 2013, doi: 10.3997/1873-0604.2014005.
[41] H. Paasche and J. Tronicke, "Nonlinear joint inversion of tomographic data using swarm intelligence," *Geophysics*, vol. 79, no. 4, pp. R133–R149, Jul. 2014, doi: 10.1190/geo2013-0423.1.
[42] D. Wilken and W. Rabbel, "On the application of particle swarm optimization strategies on Scholte-wave inversion," *Geophys. J. Int.*, vol. 190, no. 1, pp. 580–594, May 2012, doi: 10.1111/j.1365-246x.2012.05500.x.
[43] Y. Matriche, M. Feliachi, A. Zaoui, and M. Abdellah, "FDTD and improved PSO methods of coupling for identification and localization of buried objects using GPR B-scan response," *Int. J. Remote Sens.*, vol. 35, no. 21, pp. 7499–7518, 2014, doi: 10.1080/01431161.2014.968689.
[44] M. Salucci, L. Poli, N. Anselmi, and A. Massa, "Multifrequency particle swarm optimization for enhanced multiresolution GPR microwave imaging," *IEEE Trans. Geosci. Remote Sens.*, vol. 55, no. 3, pp. 1305–1317, Mar. 2017, doi: 10.1109/TGRS.2016.2622061.
[45] İ. Kaplanvural, E. Pekşen, and K. Özkap, "1D waveform inversion of GPR trace by particle swarm optimization," *J. Appl. Geophysics*, vol. 181, Oct. 2020, Art. no. 104157, doi: 10.1016/j.jappgeo.2020.104157.
[46] C. Warren, A. Giannopoulos, and I. Giannakis, "gprMax: Open source software to simulate electromagnetic wave propagation for ground penetrating radar," *Comput. Phys. Commun.*, vol. 209, pp. 163–170, Dec. 2016, doi: 10.1016/j.cpc.2016.08.020.
[47] S. D. Gedney, "An anisotropic perfectly matched layer-absorbing medium for the truncation of FDTD lattices," *IEEE Trans. Antennas Propag.*, vol. 44, no. 12, pp. 1630–1639, Dec. 1996.
[48] C. Warren *et al.*, "A CUDA-based GPU engine for gprMax: Open source FDTD electromagnetic simulation software," *Comput. Phys. Commun.*, vol. 237, pp. 208–218, Apr. 2019. [Online]. Available: http://www.sciencedirect.com/science/article/pii/S0010465518303990
[49] J. Kennedy and R. Eberhart, "Particle swarm optimization," in *Proc. Int. Conf. Neural Netw. (ICNN)*, 1995, pp. 1942–1948, doi: 10.1109/icnn.1995.488968.
[50] Y. Shi and R. C. Eberhart, "Parameter selection in particle swarm optimization," in *Proc. Int. Conf. Evol. Program.*, in Lecture Notes in Computer Science. Berlin, Germany: Springer, 1998, pp. 591–600, doi: 10.1007/BFb0040810.
[51] M. K. Sen and P. L. Stoffa, *Global Optimization Methods in Geophysical Inversion*. Cambridge, U.K.: Cambridge Univ. Press, 2013, doi: 10.1017/cbo9780511997570.
[52] I. C. Trelea, "The particle swarm optimization algorithm: Convergence analysis and parameter selection," *Inf. Process. Lett.*, vol. 85, no. 6, pp. 317–325, Mar. 2003, doi: 10.1016/s0020-0190(02)00447-7.
[53] A. Garret. (2017). *Inspyred*. Accessed: Mar. 1, 2021. [Online]. Available: https://github.com/aarongarrett/inspyred
[54] K. Deb and N. Padhye, "Development of efficient particle swarm optimizers by using concepts from evolutionary algorithms," in *Proc. 12th Annu. Conf. Genetic Evol. Comput.* New York, NY, USA: ACM, 2010, pp. 55–62, doi: 10.1145/1830483.1830492.
[55] J. L. F. Martínez, E. G. Gonzalo, J. P. F. Álvarez, H. A. Kuzma, and C. O. M. Pérez, "PSO: A powerful algorithm to solve geophysical inverse problems," *J. Appl. Geophys.*, vol. 71, no. 1, pp. 13–25, May 2010, doi: 10.1016/j.jappgeo.2010.02.001.
[56] E. Knott, *Radar Cross Section Measurements*. New York, NY, USA: Springer, 2012.
[57] D. Daniels, *Surface-Penetrating Radar* (IEE Radar, Sonar, Navigation, and Avionics Series). London, U.K.: IEE, 1996.
[58] R. Courant, K. Friedrichs, and H. Lewy, "On the partial difference equations of mathematical physics," *IBM J. Res. Develop.*, vol. 11, no. 2, pp. 215–234, Mar. 1967, doi: 10.1147/rd.112.0215.
[59] G. Blackwell, *The Electronic Packaging Handbook* (Electronics Handbook Series). Boca Raton, FL, USA: CRC Press, 2017.
[60] R. Deshpande, *Capacitors: Technology and Trends*. New York, NY, USA: McGraw-Hill, 2012.
[61] U. Kaatze, "Complex permittivity of water as a function of frequency and temperature," *J. Chem. Eng. Data*, vol. 34, no. 4, pp. 371–374, Oct. 1989, doi: 10.1021/je00058a001.

**Sam Stadler** received the M.Sc. degree in geophysics from Technical University Bergakademie Freiberg, Freiberg, Germany, in 2017.

He joined the Geoelectrics and Electromagnetics Department, Leibniz Institute for Applied Geophysics (LIAG), Hannover, Germany, in 2017. His current research interests include ground-penetrating radar (GPR) development and application in hydrogeophysics, numerical modeling of GPR antennas and GPR problems, and landmine detection.

Mr. Stadler received the Young Researcher Award of the 17th International Conference of Ground Penetrating Radar in 2018. He is part of the German Geophysical Society (DGG).

**Jan Igel** received the Diploma (M.Sc.) degree in geophysics from Karlsruhe University (KIT), Karlsruhe, Germany, in 2001, and the Ph.D. degree in geosciences from Johann Wolfgang Goethe University, Frankfurt am Main, Germany, in 2007.

He joined the Geoelectrics and Electromagnetics Department, Leibniz Institute for Applied Geophysics (LIAG), Hannover, Germany, in 2001. His current research interests include ground-penetrating radar (GPR) development and application in hydrogeophysics, sedimentology, paleoseismology, soil science, and landmine detection.

Dr. Igel is also a member of the European Geosciences Union (EGU) and the German Geophysical Society (DGG).